A 3-D coupled hydromechanical granular model for simulating the constitutive behavior of metallic alloys during solidification

M. Sistaninia [a,*], A.B. Phillion [b], J.-M. Drezet [a], M. Rappaz [a]

[a] Computational Materials Laboratory, Ecole Polytechnique Fédérale de Lausanne, Lausanne, Switzerland
[b] School of Engineering, Okanagan campus, University of British Columbia, Kelowna, Canada

Abstract

A three-dimensional (3-D) coupled hydromechanical granular model has been developed and validated to directly predict, for the first time, hot tear formation and stress–strain behavior in metallic alloys during solidification. This granular model consists of four separate 3-D modules: (i) the solidification module is used to generate the solid–liquid geometry at a given solid fraction; (ii) the fluid flow module (FFM) is used to calculate the solidification shrinkage and deformation-induced pressure drop within the intergranular liquid; (iii) the semi-solid deformation module (SDM) simulates the rheological behavior of the granular structure; and (iv) the failure module (FM) simulates crack initiation and propagation. Since solid deformation, intergranular flow and crack initiation are deeply linked together, the FFM, SDM and FM are coupled processes. This has been achieved through the development of a new three-phase interactive technique that couples the interaction between intergranular liquid, solid grains and growing voids. The results show that the pressure drop, and consequently hot tear formation, depends also on the compressibility of the mushy zone skeleton, in addition to the well-known contributors (lack of liquid feeding and semi-solid deformation).
© 2012 Acta Materialia Inc. Published by Elsevier Ltd. All rights reserved.

Keywords: Microstructure; FE modeling; Semi-solid; Discrete element method; Hot tearing

1. Introduction

Hot tearing is one of the major casting defects that occurs during the solidification of metallic alloys. Previous studies have revealed that two phenomena lead to the formation of this defect: (i) a lack of intergranular melt flow to feed solidification shrinkage and (ii) thermally induced deformations caused by the combination of solid contraction and mechanical constraints. In order for simulations to successfully predict the formation of hot tearing, both the interaction between the solid and liquid phases and the evolution in microstructure that occurs during solidification must be included. It has recently been demonstrated that partially solidified alloys can exhibit the characteristics of a cohesionless granular material, including Reynolds's dilatancy, jamming, arching and stick–slip flow [1–3]. In this regard, semi-solid behavior is quite complex in comparison with the constitutive response of solids (small strains and high stresses) and liquids (low stresses and large strains). This difference is due to the very large change in viscosity that occurs concurrently with solidification [4]. Not surprisingly, modeling hot tear formation remains a challenging task.

The standard method for investigating semi-solid mechanical behavior, and by extension hot tearing, has been to treat the semi-solid as a continuum with mechanical properties represented by averaging methods (e.g. [5–8]). The main weakness of such approaches is that they cannot account for the localization of straining and feeding at grain boundaries, a feature that has been recently clearly demonstrated by in situ X-ray tomography tensile testing experiments [3].

In the past few years, there has been interest in using granular methods in order to capture both stochastic effects and the solid–liquid interaction when simulating equiaxed globular solidification [9–11], semi-solid mechanical behavior [12–15] and liquid feeding [16–20]. In this method, the microstructure is usually approximated by polyhedral shapes based on the Voronoi diagram of a random set of nuclei, resulting in irregular grain arrangements. This approach has been used by Vernède et al. [13] to simulate the fluid flow in two dimensions caused by solidification shrinkage and grain movement, as well as by Phillion et al. [12] to investigate two-dimensional (2-D) semi-solid deformation at relatively small strains. In the latter work, the fluid was modeled as a solid material with a low elastic modulus and a small flow stress. Most recently, Sistaninia et al. have developed a series of 3-D models based on a combined finite element/discrete element method in order to investigate both the mechanical behavior of semi-solids under rather large deformations [15] and the corresponding fluid flow in a two-phase granular structure [19]. In the simulation of semi-solid deformation, the solid grains have been modeled using an elasto-viscoplastic constitutive law, while the remaining liquid films at the grain boundaries were approximated by flexible connectors. This allowed for relatively large deformations (up to $\epsilon \simeq 0.02$) to be achieved, while reducing the number of elements in the domain significantly, and avoided the issue of excessive deformation in the liquid elements seen in Ref. [12].

Although the previous granular models of solidification and semi-solid deformation have provided insight into hot tear formation, they were not successful in modelling hot tearing failure per se, i.e. the initiation and growth of a hot tear. In order to reach such a goal, the formation and percolation of voids within the intergranular liquid channels need to be considered. Furthermore, the inherent assumption of previous fluid flow models [16–20], i.e. that the grains remained fixed during solidification, needs to be addressed. In the present study, a 3-D coupled hydromechanical granular model of semi-solid deformation is developed to overcome the limitations and for the first time directly predict the formation of a hot tear in a two-phase medium. This has been achieved through development of a new three-phase interactive technique that couples the interaction between intergranular liquid, solid grains and growing voids.

2. Model development

The coupled hydromechanical granular model of semi-solid deformation is described below. It consists of four separate 3-D modules: (I) a solidification module (SM), for generating the initial solid–liquid geometry; (II) a fluid flow module (FFM), for the pressure drop calculation and localization of feeding; (III) a semi-solid deformation module (SDM), for the localization of deformation; and (IV) a failure module (FM), for modeling crack initiation and propagation. Modules II–IV are coupled together through the pressure in the liquid and the deformation of the solid in order to predict hot tear formation.

2.1. The solidification module

The solid–liquid geometry is generated using a 3-D granular solidification model known as GMS-3D [10,15]. The model is appropriate for grain-refined alloys with an equiaxed globular microstructure and assumes that the final grain structure is close to the Voronoi tessellation of random nucleation centers, as shown in Fig. 1a. To simplify the solidification calculation, the Voronoi regions are subdivided into small pyramids (see Fig. 1c), which are further divided into tetrahedral elements Fig. 1d. Because of their regular shape, solidification within a tetrahedron is reduced to a 1-D microsegregation problem, with infinite mixing in the liquid and back-diffusion in the solid. The master diffusion equation controlling the evolution of the solid–liquid interface in a tetrahedron is then given by [10]

$$v^* x^{*^2}(k_o - 1)C_\ell + \frac{1}{3}\left(L^3 - x^{*^3}\right)\frac{\dot{T}}{m_\ell} + x^{*^2}D_s\frac{\partial C_s}{\partial x}\Big|_{x^*} = 0 \qquad (1)$$

where C_s and C_ℓ are the solid and liquid composition, v^* is the solidifying velocity of the interface, x^* is its actual position, k_o is the partition coefficient, D_s is the diffusion coefficient in the solid, $\dot{T}$ is the cooling rate and m_ℓ is the slope of the liquidus line. At the end of the solidification sequence, tetrahedrons from opposing grains come into contact with each other, and coalesce.

The solidification module used in the present work contains two major modifications compared to Refs. [10,15]: coalescence and undercooling, and rounded corners.

2.1.1. Coalescence and undercooling

Coalescence during solidification corresponds to the point at which two neighboring solid grains come into contact with each other and coalesce or bridge [21]. This occurs near the end of solidification, when the width, $2h$, of the liquid layer remaining between two grains becomes on the order of the diffuse solid–liquid interfacial thickness, δ. In this granular model, the liquid channel widths diminish to a small value only by the process of solidification. However, in reality the forces applied to the grains due to hydrostatic liquid pressure and gravity can accelerate this process and cause the grains to come into contact at lower g_s. Solidification of this last liquid film depends on the interfacial energies of the (dry) grain boundary, γ_{gb}, and of the solid–liquid interface, $\gamma_{s\ell}$. As shown by Rappaz et al. [21], the coalescence undercooling ΔT_b in a pure material required to have a dry boundary is given by

$$\Delta T_b = \frac{\gamma_{gb} - 2\gamma_{s\ell}}{\Delta s_f}\frac{1}{\delta} \qquad (2)$$

where Δs_f is the entropy of fusion per unit volume. γ_{gb} varies between 0 and $\gamma_{gb,max}$ as a function of grain misorientation $\Delta\theta$, and is shown in Fig. 2a for a [1 0 0] symmetric tilt
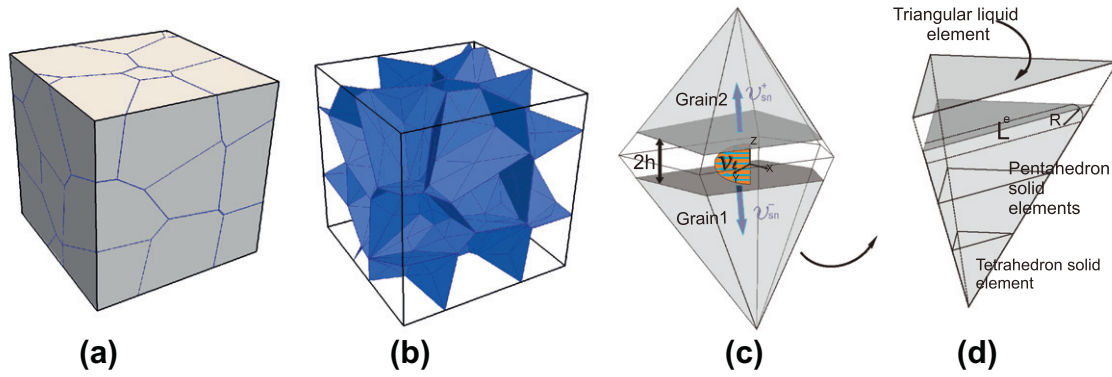
Fig. 1. The domain of the granular semi-solid model: (a) the entire model domain containing 27 (3 × 3 × 3) grains; (b) the network of the triangular liquid elements in between the polyhedral grains; (c) liquid velocity profile in between two facets of two neighbor grains; and (d) a single tetrahedron decomposed into a set of solid elements.
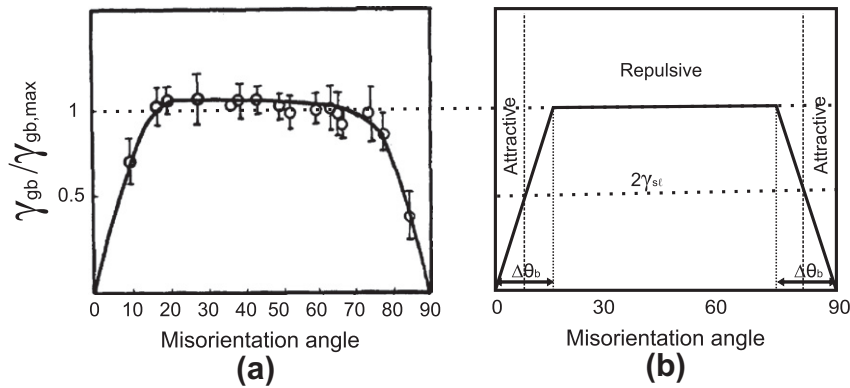

Fig. 2. Relative grain boundary energy as a function of misorientation: (a) measured for symmetric [001] tilt boundaries in 99.998% Al [22]; (b) the function used in the SM.

boundary of 99.998% Al [22]. Note that, in this figure, $\gamma_{s\ell}$ has been given an arbitrary value for illustrative purposes. For small-angle grain boundaries, $\gamma_{gb} < 2\gamma_{s\ell}$, and the interfaces are attractive. In this case, coalescence is associated with a decrease in free energy and will occur as soon as the two solid–liquid interfaces begin to impinge. Alternatively, for large-angle grain boundaries, $\gamma_{gb} > 2\gamma_{s\ell}$ and the interfaces are repulsive. Thus the thermal undercooling, ΔT_b of Eq. (2), will be required to provide the driving force for coalescence. For an alloy, it has been shown that coalescence is achieved once the composition of the remaining liquid film reaches a coalescence line parallel to and ΔT_b below the liquidus [21].

Although the classification of grain misorientation in three dimensions generally requires five independent parameters (three for misorientation of the crystal lattice and two for the orientation of the grain boundary plane), the statistical effects of coalescence are captured in the present study by randomly assigning a single orientation value between 0 and 90° to each grain. The misorientation is then calculated ($\Delta\theta = \theta_1 - \theta_2$) and translated into γ_{gb} based on Fig. 2b. The key adjustable parameter is the critical misorientation angle $\Delta\theta_b$ at which $\gamma_{gb} = \gamma_{gb,max}$, since this will affect the number of attractive and repulsive boundaries,

and hence coalescence, in the bulk. The value of $\Delta\theta_b$ has been determined through trial and error by comparing the mechanical response of the system to an imposed displacement to the tensile experimental data available in the literature [8,23]. As will be shown in Section 3, a good agreement is found with $\Delta\theta_b = 10°$. This fitting parameter could be eliminated if a distribution of grain boundary energy as a function of grain misorientation and grain boundary normal direction (i.e. five angles) were available in the literature. Unfortunately, such is not the case, so a simple distribution based on a pure tilt boundary with an adjusted value of $\Delta\theta_b$ has been used in the present case.

2.1.2. Rounded corners

One major drawback with the use of a Voronoi tessellation to generate the microstructure is that the resulting grains contain the sharp edges and vertices of the corresponding polyhedra. In real semi-solid microstructures, metallic alloys are non-faceted crystals and have a smooth surface. The result of these sharp features is that liquid pockets do not form at the grain triple lines and vertices and hence this geometry overestimates the volume fraction of solid at which coalescence occurs as compared to experiments [8,24]. To improve the granular solidification simu-

lation, an approximation for the radius of curvature previously developed by Vernède and Rappaz [25] has been added to the GMS-3D software as part of the present study. Note that, as this equation was derived to round the corners of a polygonal grains in two dimensions, the corresponding geometric correction in three dimensions is to round the grains along the edges (triple lines) of the Voronoi tessellation, and consequently rounding at the vertices is ignored. The approximation derived in Ref. [25] was based on a solute balance between the solute flux induced by the Gibbs–Thomson effect and the geometrical advantage of a rounded corner for diffusion. The radius of curvature at the grain corner (or triple line) is given by

$$R = \left[A_c \frac{2}{\tan\alpha - \alpha} \frac{\Gamma_{s\ell} D_\ell}{-\dot{T}} \right]^{1/3} \tag{3}$$

where A_c is a dimensionless constant, α is half of the supplementary angle of the grain corner angle and $\Gamma_{s\ell}$ is the Gibbs–Thomson coefficient. The volume of liquid that is added due to the rounded edges is then given by

$$\mathcal{V} = R^2 L_e (\tan\alpha - \alpha) \tag{4}$$

where L_e is the length of the edge (see Fig. 1d).

Since the addition of grain rounding increases the overall volume of liquid in the domain, the value of x^* must be moved slightly forward to maintain a constant fraction of solid. Hence, coalescence occurs at a lower solid fraction than with the sharp interface method. The width of the liquid layer considered for the coalescence calculation is then given by

$$2h^* = 2h - 2\left[2A_c \frac{\Gamma_{s\ell} D_\ell}{-\dot{T}} \right]^{2/3} \frac{\sum_{i=1}^{n} L_e^i [\tan\alpha^i - \alpha^i]^{1/3}}{\sum_{i=1}^{n} S_{s\ell}^i} \tag{5}$$

where $i = 1, 2, \ldots, n$ are the edges of the two neighboring facets, $S_{s\ell}$ is the solid–liquid interfacial area of the tetrahedron and $2h$ is the width of the liquid channel computed by the flat interface method (see Fig. 1d).

2.2. Fluid flow module

Intergranular fluid flow during solidification occurs mainly due to volumetric shrinkage related to the phase change and mechanical deformation, with the feeding and straining localization and reduction in fluid flow at high solid fraction being key factors in hot tear formation. The fluid flow module is based on previous work [19], utilizes the semi-solid geometry from the SM and assumes that the flow between the solidifying polyhedral grains is parallel to their facets, i.e. the fluid velocity $\vec{v}_\ell$ has only two components, $v_{\ell x'}$ and $v_{\ell y'}$, in a frame attached to the solid facet, with the local z'-axis perpendicular to it (see Fig. 1c). The Navier–Stokes equation with these assumptions leads to the Poiseuille flow formulation between two parallel plates,

$$\vec{v}_\ell = \frac{1}{2\mu_\ell} \vec{\nabla} p_\ell [z'^2 - h^2] \tag{6}$$

where p_ℓ is the pressure and μ_ℓ is the dynamic viscosity of the liquid. As shown in Ref. [19], the Poiseuille flow assumption is reasonable for fluid flow in a representative volume element (RVE) at $g_s > 0.80$ [19]. Considering Eq. (6) with a local mass balance, it has been shown in Ref. [19] that the pressure in the liquid is given by

$$\frac{2h^3}{3\mu_\ell} \nabla^2 p_\ell = 2\beta v^* + \Delta v_{sn} + \frac{2h}{K_\ell} \frac{\partial p_\ell}{\partial t} \tag{7}$$

where $\beta = (\rho_s/\rho_\ell - 1)$ is the shrinkage factor, ρ_s and ρ_ℓ are the densities of the solid and of the liquid, v^* is the solidification speed of the solid–liquid interface and $\Delta v_{sn} = v_{sn}^+ - v_{sn}^-$ is the normal velocity difference of the solid grains. If $\Delta v_{sn} > 0$, this induces a liquid suction, while for $\Delta v_{sn} < 0$ liquid is expelled from the interface. The last term in Eq. (7) has been added as compared to Ref. [19] in order to handle numerically isolated liquid pockets, with K_ℓ being the bulk modulus of the liquid. Thus, the left-hand side of Eq. (7) provides the variation of pressure required to compensate both the solidification shrinkage and the solid deformation on the right-hand side. At a high solid fraction and/or when feeding is poor, this term is very small and the fluid loss due to solidification shrinkage and solid deformation is compensated by a reduction in ρ_ℓ via the third term on the right-hand side.

A finite element code [19] has been implemented as part of GMS-3D to solve Eq. (7) and thus to calculate the liquid pressure in the semi-solid medium. Since the flow within an element has been assumed to be parallel to the facets only, the 3-D prismatic geometry within which it occurs is further reduced to 2-D three-node triangular elements (see Fig. 1c) using the Galerkin method. The global stiffness matrix is solved with a conjugate gradient linear iterative method using a free open-access program C++ template library known as IMIL++ [26].

2.3. The semi-solid deformation module

The second key factor in hot tear formation is the deformation of the solid skeleton. The geometry for simulating semi-solid deformation consists of the solid grains from the SM surrounded by liquid channels. Within each grain, deformation is rather homogeneous and modeled using a continuum FE method, whilst, within the entire domain, discontinuous deformation is modeled using the discrete element method. As shown previously, the SDM requires a domain containing a minimum of 700 grains in order to accurately model semi-solid deformation [27]. Above this number, the behavior of the domain does not depend on the number and/or the distribution of grains, i.e. the domain can be considered as an RVE of the mushy zone. To perform the simulation, the geometry of the SM is transformed into an FE mesh using a C++ subroutine within GMS-3D. Each solid tetrahedron is further split into three elements (a tetrahedron and two pentahedrons, as shown in Fig. 1d). As a result, the FE mesh consists of approximately 120 solid elements per grain. The numerical simulation of

the SDM is then performed using the commercial code Abaqus 6.9TM using an elasto-viscoplastic constitutive law to control deformation of the solid phase. The flow stress is based on the viscoplastic Ludwik's equation,

$$\sigma(\varepsilon, \dot{\varepsilon}, T) = k_s(T)\varepsilon^{n(T)}\dot{\varepsilon}^{m(T)} \tag{8}$$

where σ is the stress, ε is the total plastic strain experienced by the material, $\dot{\varepsilon}$ is the strain rate, k_s is a flow stress coefficient, n is the strain hardening parameter and m is the strain rate sensitivity of the material. Prior to coalescence, the neighboring grains are connected to each other via elastic connector elements. Furthermore, a frictionless hard contact pressure–overclosure relationship is used to prevent solid grain penetration. This formulation is similar to that of our previous model [15], but with a negligible stiffness coefficient assigned to the connectors as compared to the resistance due to liquid pressure. Instead, it is assumed that the resistance of the liquid channels to separation prior to coalescence is due only to the pressure that is exerted on the solid–liquid interfaces and calculated by the FFM.

2.4. The failure module

In order to model hot tear formation directly, a criterion for this defect's initiation and propagation is necessary. Assuming that there is contact between the liquid and the atmosphere, which is the case in the semi-solid tensile tests used to measure mechanical strength (e.g. [28]) and to investigate hot tearing (e.g. [3]), the criterion can be estimated from the overpressure required to overcome capillary forces at the liquid–atmosphere interface, as illustrated in Fig. 3. Further, assuming cylindrical geometry (i.e. the second principal curvature is nil, $\kappa_2 = \frac{1}{R_2} = 0$ [29]), the Young–Laplace equation of the penetrating void is given by

$$p_a - p_\ell = \frac{\lambda}{R_1} = \frac{\lambda \cos \Theta}{h} \tag{9}$$

where p_a is the atmospheric pressure, Θ is the dihedral angle and λ is the surface tension at the void–liquid interface. Considering that a thin oxide skin has formed between the atmosphere and the liquid, the value of λ can be estimated as [30]
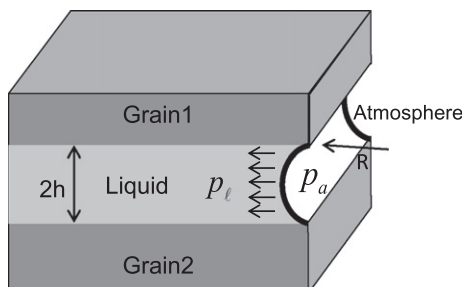

Fig. 3. Schematic of two grains and a liquid channel within which a meniscus with a hemi-cylindrical shape starts forming.

$$\lambda = \gamma_{\ell o} + \gamma_{og} + \tau\delta \tag{10}$$

where $\gamma_{\ell o}$ and γ_{og} are the interfacial energies[1] between oxide skin and liquid and between oxide skin and air, respectively, and δ and τ are the thickness and the tensile strength of the oxide layer. For simplification, the $\lambda \cos \Theta$ value has been fixed to 5 J m^{-2} in the present simulations [30]. Thus, the hot crack starts to propagate into a liquid channel connected to the atmosphere once p_ℓ is such that

$$p_\ell = p_a - \frac{5}{h} \ (\text{Pa}) \tag{11}$$

Since the width of the widest channel h_{max} increases during a semi-solid tensile test, the maximal p_ℓ within the widest channel, i.e. $p_{\ell,max}^c = p_a - \frac{5}{h_{max}}$ also increases during tensile deformation.

Once the oxide layer of a channel between the liquid and the atmosphere has been broken, the crack propagates abruptly into the corresponding channel and later into the channels connected to it. The oxide layer formed during the crack propagation process is extremely thin and thus can be ignored, allowing for the assumption of $\lambda = \gamma_{g\ell}$, where $\gamma_{g\ell}$ is the interfacial energy between liquid and air. Experimental investigations have also verified that the value of λ for a newly formed oxide layer is close to $\gamma_{g\ell}$, i.e. $\simeq 1$ J m^{-2} [30]. In the present model, it is assumed that the crack propagation into a channel connected to the crack tip satisfies the condition

$$p_\ell \leqslant p_a - \frac{2}{h} \ (\text{Pa}) \tag{12}$$

2.5. Hydro-mechanical coupling

To simulate hot tear formation and propagation, the FFM, SDM and FM modules are coupled as shown in Fig. 4. This occurs by carrying out each of the FFM, SDM and FM simulations incrementally at a given solid fraction (i.e. SM output), with iterations between each increment, until overall failure occurs. Assuming an initial value for liquid pressure $p_\ell = p_{\ell 0}$, the simulation begins with the SDM calculation. The mechanical response of the system to the imposed displacement $\Delta u_v = \dot{\varepsilon}_v L \Delta t$, where $\dot{\varepsilon}_v$ is the bulk strain rate and L the dimension of the RVE, is calculated and then imported into the FFM. The new thickness $2h$ and the value Δv_{sn} are then calculated for all channels using the normal strain, $\varepsilon_{z'}$, of each liquid film from the SDM. With this information, the pressure p_ℓ is calculated using the FFM. The liquid pressure, p_ℓ, calculated with FFM is imported to the SDM for the next iteration and the iterations are continued until the p_ℓ values converge (i.e. $|p_\ell - p_{\ell 0}| < Tol$ where Tol is a tolerance factor).

---

[1] Although the oxide skin is a solid, we assume that surface tension and surface energy are equal.

Fig. 4. Flow chart outlining the sequentially coupled calculation.

Table 1
List of parameters used in the calculation (relevant for Al–Cu alloys).

Parameter	Value	Parameter	Value
ρ_ℓ	2440 kg m^{-3} [13]	μ_ℓ	1.5×10^{-3} Pa s [13]
K_ℓ	41 GPa [31]	β	0.074 [13]
Δs_f	1.02×10^6 J K^{-1} m^{-3} [11]	$\Gamma_{s\ell}$	5×10^{-7} K m [25]
D_s	1.5×10^{-13} m^2 s^{-1} [25]	D_ℓ	3×10^{-9} m^2 s^{-1} [32]
$\gamma_{gb,max}$	0.324 J m^{-2} [11]	$\gamma_{s\ell}$	0.092 J m^{-2} [11]
E_{solid}	30 GPa [33]	ν_{solid}	0.30 [33]
m	0.164 [34]	n	0.022 [34]
k_s	30.5 MPa s^m [34]		

condition has been applied to the surfaces $x = 0$, $y = 0$ and $z = 0$ of the RVE. The surface $x = L_x$ is connected to a reference node that is displaced at a fixed velocity in the x-direction, while the surfaces $y = L_y$ and $z = L_z$ are free to move. The variables L_x, L_y and L_z refer to the dimensions of the domain in the x, y and z directions, respectively.

3.1. Feedable mushy zone

The feedable RVE represents the industrial scenario seen in aluminum alloy DC casting. In order to feed the RVE at a given g_s, the liquid metal first traverses the rest of the mushy zone at lower g_s. The proper boundary condition where liquid feeding is allowed is thus the so-called Robin boundary condition,

$$\phi = f_\ell(p_\ell - p_m) \tag{13}$$

where ϕ is the liquid flux, f_ℓ is the feeding coefficient and p_m is the metallostatic pressure at $g_s = 0.0$. Using Darcy's law, f_ℓ is calculated as a function of g_s,

$$f_\ell = \frac{\phi}{p_\ell - p_m} = \frac{1}{\int_{T_\ell}^{T} \frac{\mu_\ell(1 - g_s(T))}{\mathcal{K}(g_s)G} dT} \tag{14}$$

where T_L is the liquidus temperature, $\mathcal{K}$ is the permeability of the mushy zone and G is the thermal gradient. The feeding ability of the RVE decreases with f_ℓ, so that $f_\ell = 0$ corresponds to a closed boundary. However, as f_ℓ approaches infinity, the boundary condition approaches a Dirichlet boundary condition, i.e. $p_\ell = p_m$ (imposed pressure). Fig. 5 shows a comparison of the variation in f_ℓ with g_s for three different thermal gradients. In the calculation of this figure, the evolutions of $g_s(T)$ and $\mathcal{K}(g_s)$ have been calculated using the solidification module and the Carman–Kozeny relationship [19,35], respectively. As can be seen, the feeding ability of the mushy zone at high g_s and near the end of solidification is, as expected, very low due to its low permeability.

The simulated tensile behavior of the RVE for $g_s = 0.98$ at various values of $\dot{\varepsilon}_v$ and f_ℓ is shown in Fig. 6, with (a) providing the average stress, predicted with SDM, and (b) providing the average liquid pressure, predicted by the FFM, over the surface $x = L_x$ during the tensile deformation. In these simulations, all of the surfaces of the RVE are closed except the surface $x = 0$, where feeding is allowed and is given by Eq. (13) (p_m is set to zero). As

Once convergence is reached, the pressure in a channel is compared to the failure criterion of the FM. When a hot tear forms in a channel, its liquid is sucked into the rest of the liquid network and the channel becomes open and dry. Hence, when the FM predicts that a hot tear has formed in a given channel, the pressure in this channel is set to p_a for the SDM calculation of the next increment. However, it no longer contributes to the overall feeding in the FFM calculation and the channel is closed by setting its displacement (local deformation) to $-2h$ ($\varepsilon_{z'} = -1$) for the next increment. Time is then incremented, and the process is repeated for the new displacement Δu_v.

3. Results and discussion

The simulations presented below investigate the effects of fluid flow and deformation on hot tearing at a constant g_s in an Al–2 wt.% Cu alloy. The physical parameters used in the computations are given in Table 1. First, the behavior of a feedable mushy zone, such as that found in direct chill (DC) casting, is presented. Secondly, the behavior of an unfeedable mushy zone, which is the case in semi-solid tensile tests (e.g. [3,8,23]), is investigated. Thirdly, the model results are validated against bulk experimental data available in the literature [8,23]. These simulations have been performed using a 1000-grain domain ($10 \times 10 \times 10$) with a grain size of 100 μm, a cooling rate of -1 K s^{-1} and $\Delta\theta_b = 10°$ unless otherwise stated. For the FFM calculation, p_a is assumed to be zero. For the SDM calculation, a symmetry boundary
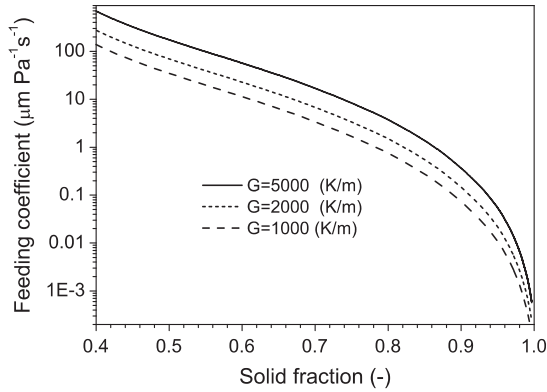
Fig. 5. Variation in feeding coefficient f_ℓ for Al–2 wt.% Cu alloy with g_s for three different thermal gradients.
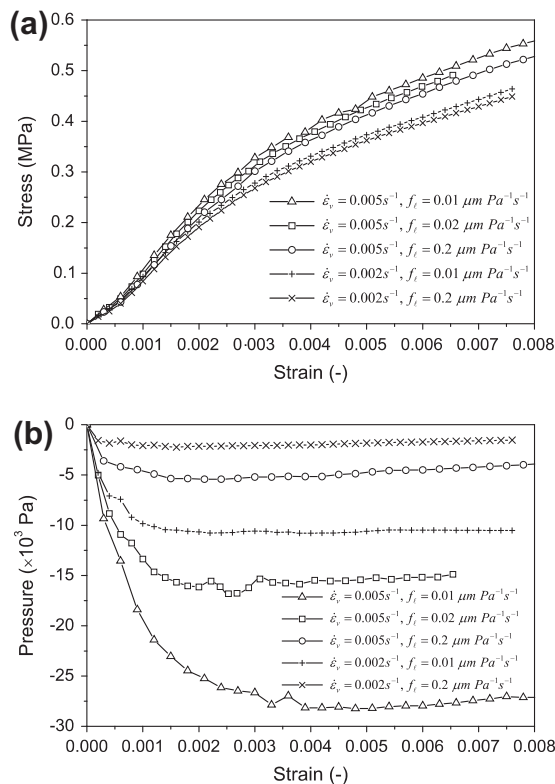

Fig. 6. Simulated tensile behavior with liquid feeding of a partially solidified Al–2 wt.% Cu alloy at $g_s = 0.98$ for different strain rates and different feeding coefficients: (a) stress vs. strain curves; (b) liquid pressure vs. strain curves.

can be seen, the liquid pressure is not low enough to significantly affect the result of the SDM and thus the stress shows only a minor dependence on f_ℓ. When $f_\ell = 0.2 \ \mu m \ s^{-1} \ Pa^{-1}$, the liquid pressure seems to be mainly a function of $\dot{\varepsilon}_v$. However, for the curves at lower f_ℓ ($f_\ell = 0.02 \ \mu m \ s^{-1} \ Pa^{-1}$ and $0.01 \ \mu m \ s^{-1} \ Pa^{-1}$), the liquid pressure is also a function of the strain ε_v, a feature which cannot be addressed by averaging techniques.

Considerable effort has been devoted to understanding the hot tearing phenomenon (see the review by Eskin et al. [36]). Several hot tearing theories have been suggested

based on the strain accumulation at the hot spot, yet other authors have argued that it is not the strain but the strain rate which is the critical parameter for hot cracking. As can be deduced from the results of this model, the critical parameter depends on the feeding conditions of the mushy zone. The hydrodynamic behavior of the mushy zone can be divided into two regimes. At high f_ℓ, the liquid pressure drop in the mushy zone is a function of only the strain rate. However, at lower f_ℓ, it is also a function of strain and, as f_ℓ decreases, the pressure-drop dependency on ε_v increases.

Fig. 7 shows pressure contours within the RVE for different values of $\dot{\varepsilon}_v$ and f_ℓ, outlined in Fig. 6, when the overall or bulk strain is 0.005. Comparing Fig. 7b and c, although the local pressure decreases with f_ℓ, the difference between the maximum and minimum pressures shown in the legend remains constant. This is because the pressure gradient in the RVE is a function only of $\dot{\varepsilon}_v$ and does not depend on f_ℓ. When f_ℓ is extremely low or zero, the difference between the maximal and minimal pressures in such a small RVE is very small, in comparison with the average pressure drop, and allows one to simply assume that the pressure input into the SDM calculation is uniform. Furthermore, the liquid pressure is substantially higher than the cavitation pressure[2] in the narrow liquid channels ($p^c_{\ell,max} \simeq -2$ MPa, calculated with Eq. (11) for the widest channel) and it cannot lead to hot tearing. Thus, in order for hot tearing to occur in a fully saturated mushy zone with an average grain size of 100 μm, the semi-solid permeability must be considerably lower than the values predicted by the Carman–Kozeny relationship.

3.2. Unfeedable mushy zone

The externally unfeedable RVE represents the scenario seen in aluminum alloy semi-solid tensile tests. Fig. 8a shows the stress–strain predictions for three values of g_s (0.92, 0.96 and 0.98), at a strain rate of $\dot{\varepsilon}_v = 0.001 \ s^{-1}$, under the assumption that all of the surfaces of the RVE are closed for the FFM calculation. As can be seen, the stress increases with increasing strain, as expected, and reaches a maximum value σ_{max} before overall failure occurs. Since the RVE is not fed by incoming liquid and both the liquid and solid phases are nearly incompressible, the liquid pressure drops. This depression leads to a contraction of the RVE in the two dimensions normal to the tensile loading, with the contraction being such that the overall domain volume remains nearly constant. Thus, the liquid depression within the RVE is dictated by the compressibility of the mushy zone skeleton and, as g_s increases, this compressibility will decrease, resulting in a larger liquid pressure drop.

The pressure drop in the intergranular liquid that occurs during tensile deformation is reported in Fig. 8b

---

[2] Cavitation here means the pressure at which a pore grows in the widest channel, assuming nucleation to be very easy.
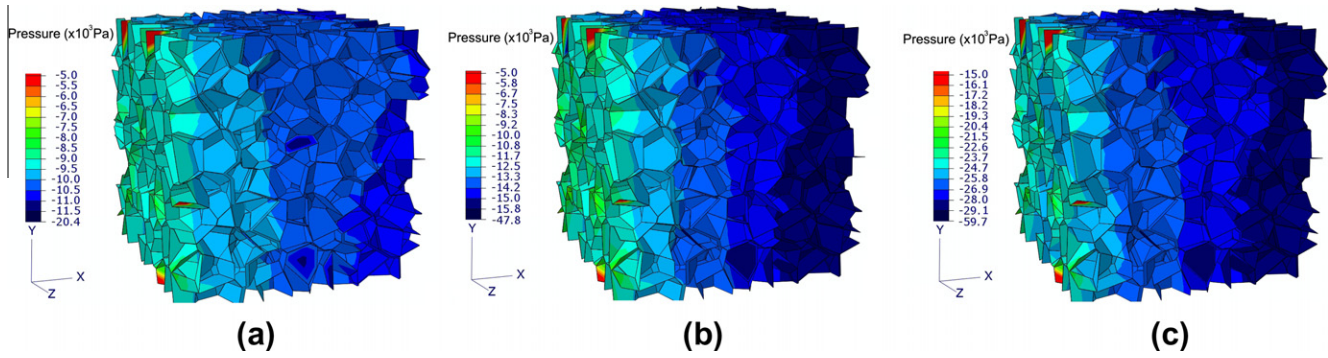
Fig. 7. Contour plots of the liquid pressure at $\varepsilon_v = 0.005$ and $g_s = 0.98$ for (a) $f_\ell = 0.01$ μm s^{-1} Pa^{-1}, $\dot{\varepsilon} = 0.002$ s^{-1}, (b) $f_\ell = 0.02$ μm s^{-1} Pa^{-1}, $\dot{\varepsilon} = 0.005$ s^{-1} and (c) $f_\ell = 0.01$ μm s^{-1} Pa^{-1}, $\dot{\varepsilon} = 0.005$ s^{-1}, corresponding to Fig. 6.
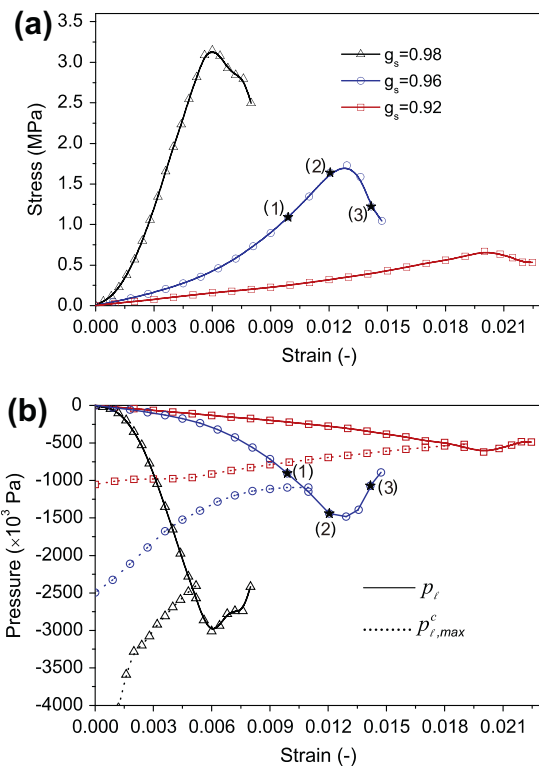
Fig. 8. Simulated tensile behavior without liquid feeding of a partially solidified Al–2 wt.% Cu alloy for various solid fractions: (a) stress vs. strain curves; (b) pressure vs. strain.

(continuous curves, output of the FFM), along with the failure pressure $p^c_{\ell,max}$ associated with the widest channel (dashed curves, output of the FM). As can be seen, the liquid pressure drop at $g_s = 0.98$ is approximately six times larger that for $g_s = 0.92$. The two curves p_ℓ and $p^c_{\ell,max}$ cross at the strains $\varepsilon_v = 0.0047$, $\varepsilon_v = 0.0107$ and $\varepsilon_v = 0.0185$ for $g_s = 0.98$, $g_s = 0.96$ and $g_s = 0.92$, respectively. Consider the curves corresponding to $g_s = 0.96$. At the point of intersection, which is one increment beyond location (1), the first cracks have now initiated in the wider channels connected to ambient air. As can be seen by comparing this portion of the curves in Fig. 8a and b, the overall stress within the RVE continues to increase, but at a lower rate.

With increasing strain, the cracks continue to propagate within the RVE, and the rate $d\sigma_v/d\varepsilon_v$ continues to decrease until σ_{max} is reached one increment beyond (2), when the rate becomes negative. In other words, crack initiation occurs prior to σ_{max} being reached. The increase in p_ℓ observed after point (2) is due to crack propagation which relaxes the pressure drop. As discussed previously, the liquid present in a channel that becomes dry due to crack propagation is sucked into other regions of the mushy zone. During an increment Δt, this quantity of liquid is given by

$$Q = \frac{\sum_{i=1}^{n} V_\ell^i}{\Delta t} \qquad (15)$$

where $V_\ell^i (i = 1, 2 \ldots, n)$ is the volume of the prismatic element i where a hot tear has formed during the increment. Once Q reaches approximately $\dot{\varepsilon}_v(L_x \times L_y \times L_z)$, the pressure drop stops increasing, since, at this point, the liquid provided by the propagating cracks is sufficient for feeding deformation. Thereafter, p_ℓ becomes equal to $p^c_{\ell,max}$ and, since the $p^c_{\ell,max}$ increases during tensile deformation, p_ℓ also starts to increases.

The σ_{max} depends heavily on the strength of the oxide layer, i.e. the factor $\lambda\cos\Theta = 5$ J m^{-2} in Eq. (11), and to a lesser extent on the growth factor 2 in Eq. (12). In order to assess the influence of this factor on σ_{max}, the simulation of deformation at $g_s = 0.96$ has been repeated for two other values of this factor. From these simulations, the variation in σ_{max} is as follows:

1. $\sigma_{max} = 1.23$ MPa for $\lambda\cos\Theta = 3$ J m^{-2},
2. $\sigma_{max} = 1.70$ MPa for $\lambda\cos\Theta = 5$ J m^{-2},
3. $\sigma_{max} = 1.98$ MPa for $\lambda\cos\Theta = 7$ J m^{-2}.

As can be seen, the maximum strength of the RVE increases as a function of the strength of the oxide layer, as a result of the increase in the pressure depression required to developing cracks within the RVE.

Fig. 9 shows the contour plots of the Von Mises stress (in MPa) at a slice inside the RVE for $g_s = 0.96$ at the three strains corresponding to (1), (2) and (3) in Fig. 8. In this figure, the channels in which the Von Mises stress is not
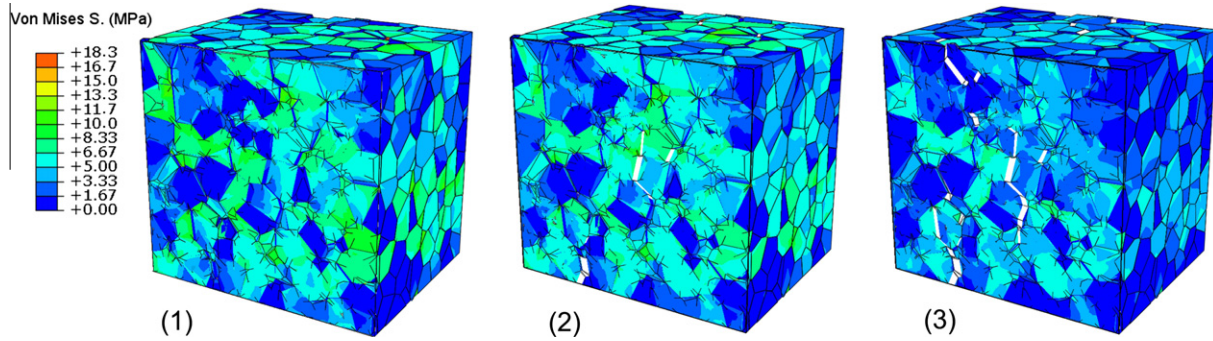
Fig. 9. Contour plots of the Von Mises stress at the three strains corresponding to (1), (2) and (3) of Fig. 8 and for $g_s = 0.96$. The white channels correspond to those where a hot tear has formed.

represented are shown as white and correspond to those where a hot tear has formed. Since the overpressure required for initiation of a new crack (Eq. (11)) is lower than the pressure required for crack propagation inside the RVE (Eq. (12)), the cracks propagate within the RVE rather than over the outer surfaces of the RVE. As can be seen, the stress in the percolated grains is significantly higher than its value in the other grains. The percolated grains transmit the portion of the load transmitted by solid skeleton from the left to the right face of the RVE. As the cracks propagate within the RVE, the stress in the RVE is finally released.

3.3. Model validation

In Fig. 10, a comparison is made between the simulated stress–displacement predictions and the experimental results for the same Al–2 wt.% Cu alloy [8] in order to validate the simulations over a range of g_s between 0.92 and 0.98 at a strain rate of $\dot{\varepsilon}_v = 0.001 \text{ s}^{-1}$. In order to make such a computation, it is first necessary to account for the axial thermal gradient present in the experiments of Ludwig et al. [8]. The overall displacement u_v imposed to the specimen is in fact accommodated preferentially by the weakest zone of the mushy zone, i.e. that with the highest temperature, T_{max} (or lowest solid fraction, $g_{s,min}$). Thus, the total displacement can be written as

$$u_v = \int_{z_{min}}^{z_{max}} du_v(z) = \int_{g_{s,min}}^{1} \frac{du_v}{dz} \frac{dz}{dg_s} dg_s \qquad (16)$$

Based on thermal measurements made on a nondeformed specimen [8], the local strain $\frac{du_v}{dz}(g_s)$ for a given tensile stress σ_v has been calculated using the strain–stress curves obtained for different uniform g_s values (Fig. 8a). The total deformation of the specimen (u_v) for various values of σ_v can then be predicted using the Eq. (16), as shown in Fig. 10. As can be seen, this model is able to correctly reproduce the general trends of the experimental curves for the four values of g_s. It can also be seen that both the experimental data and the simulations exhibit a convex shape $\sigma_v(\varepsilon_v)$ prior to failure with an increasing rate $d\sigma_v/d\varepsilon_v$ despite the alloy being elastic–perfectly plastic at
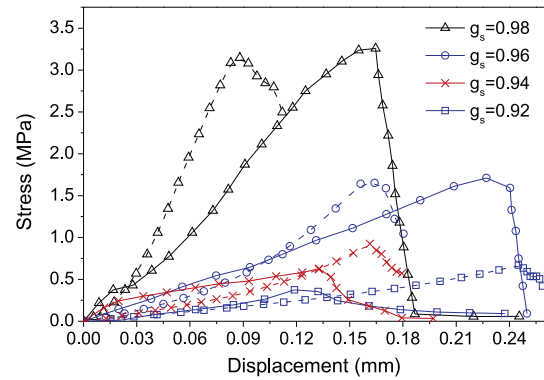

Fig. 10. Comparison of simulated (dashed lines) and experimental (continuous lines) tensile behavior [8] of partially solidified Al–2 wt.% Cu alloy at various solid fractions: □ $g_s = 0.92$ ($T = 883 \text{ K}$); × $g_s = 0.94$; ○ $g_s = 0.96$ ($T = 858 \text{ K}$); △ $g_s = 0.98$ ($T = 824 \text{ K}$).

$g_s = 1$ [8,34]. In the present simulation, the hardening behavior can be understood by considering the liquid pressure–strain behavior (Fig. 8b): the rate $-dp_\ell/d\varepsilon_v$ is increasing, thus leading to an increase in the rate $d\sigma_v/d\varepsilon_v$ and consequently the convex shape $\sigma_v(\varepsilon_v)$.

The model predictions at different strain rates have also been validated by comparing them against experimental data from Ref. [23], which also used an Al–2 wt.% Cu alloy. These data were obtained using a rig test [37] in which deformation was localized to the central part of the sample (approx. 40 mm in length). The temperature of the hot zone, assumed to be uniform, was about $T = 813 \text{ K}$. As can be seen in Fig. 11, the results of the model reproduce the general trends of the experimental curves, obtained at strain rates of 0.001 s^{-1} and 0.004 s^{-1}, quite accurately. Note that the experimental data consist of two stress–strain curves at each strain rate, and show a fairly large dispersion concerning the maximum strain before failure.

Finally, the bulk stress–strain curves obtained for various values of $\Delta\theta_b$ ($\Delta\theta_b = 6°$, 11° and 14°) are shown in Fig. 12 in order to assess the influence of this parameter. As can be seen, $\Delta\theta_b$ has a strong influence on the stress–strain behavior. In addition, the percolation of the solid phase for the three values of $\Delta\theta_b$ has been determined, with
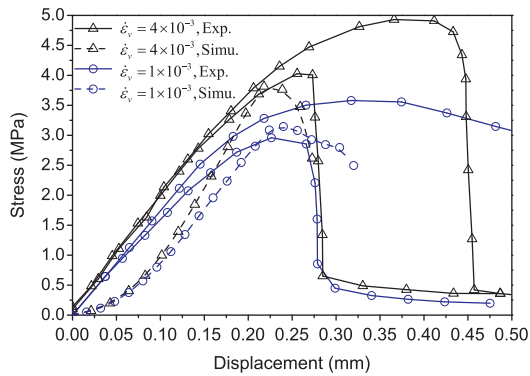
Fig. 11. Comparison between tensile experimental results (continuous curves) [23] and simulation results (dashed line curves) of partially solidified Al–2 wt.% Cu alloys as a function of strain rate ($\dot{\varepsilon}_v$(0.001 s^{-1} and 0.004 s^{-1})) at $g_s = 0.98$.
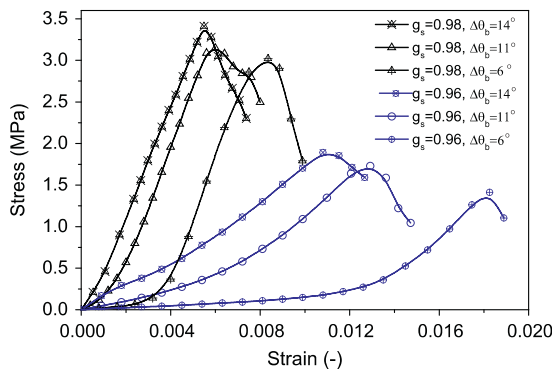

Fig. 12. Comparison between simulated stress–strain curves showing the effects of $\Delta\theta_b$ at two different values of g_s (0.96 and 0.98).

percolation being defined as the solid fraction for which a continuous path of solid (across only coalesced grain boundaries and not liquid films) is present from one side of the RVE to the other. The solid fraction for percolation in these simulations is calculated to be $g_{s,perc}$=0.995, 0.95 and 0.90 for $\Delta\theta_b = 6°$, 11° and 14°, respectively. There is therefore a strong link between the $g_{s,perc}$ and $\Delta\theta_b$ that results in the variation in stress–strain behavior seen in Fig. 12.

4. Conclusion

A 3-D granular hydromechanical coupled model has been developed to predict hot tearing formation in solidifying alloys. This model is made up of four separate 3-D modules; (I) a solidification module, (II) a semi-solid deformation module, (III) a fluid flow module and (IV) a failure module. This model is able to predict the overall response of semi-solid alloys to an externally applied strain before and after fracture initiation, while accounting for the localization of strains at grain boundaries. The stress–strain predictions of this model have been validated against experimental data available in the literature, and agree well with the experimental results. The results of the analysis

demonstrate that, when a feedable mushy zone is present, the hydrodynamic behavior and consequently the hot tearing behavior of semi-solid alloys can be divided into two regimes: (I) at high feedability, the liquid pressure drop is a function of strain rate only, and (II) at low feedability, the pressure drop is both a function of strain and strain rate. When the mushy zone cannot be fed, the pressure drop and thus the sensitivity to hot tearing depend on the compressibility of the mushy zone skeleton in addition to deformation of the semi-solid. The low compressibility in semi-solids that are not able to be properly fed lead to a huge pressure drop and consequently to the formation of hot tears.

Acknowledgements

References

[1] Gourlay CM, Dahle AK. Nature 2007;445:70.
[2] Gourlay CM, Dahle AK, Nagira T, Nakatsuka N, Nogita K, Uesugi K, et al. Acta Mater 2011;59:4933.
[3] Terzi S, Salvo L, Suèry M, Limodin N, Adrien J, Maire E, et al. Scripta Mater 2009;61:449.
[4] Dantzig JA, Rappaz M. Solidification. EPFL Press; 2009.
[5] Bernard D, Nielsen O, Salvo L, Cloetens P. Mater Sci Eng A – Struct Mater Properties Microstructure and Processing 2005;392:112.
[6] Monroe C, Beckermann C. Mater Sci Eng A 2005;413–414:30.
[7] M'Hamdi M, Mo A, Martin C. Metall Mater Trans A 2002;33:2081.
[8] Ludwig O, Drezet JM, Martin C, Sury M. Metall Mater Trans A 2005;36:1525.
[9] Vernède S, Rappaz M. Philoso Mag 2006;86:3779.
[10] Phillion AB, Desbiolles JL, Rappaz M. Modeling of casting, welding, and advanced solidification processes, vol. XII. Warrendale (PA, USA): Minerals, Metals & Materials Soc; 2009. p. 353–60.
[11] Mathier V, Jacot A, Rappaz M. Model Simul Mater Sci Eng 2004;12:479.
[12] Phillion AB, Cockcroft SL, Lee PD. Acta Mater 2008;56:4328.
[13] Vernède S, Dantzig JA, Rappaz M. Acta Mater 2009;57:1554.
[14] Lahaie DJ, Bouchard M. Metall Mater Trans B 2001;32:697.
[15] Sistaninia M, Phillion A, Drezet JM, Rappaz M. Metall Mater Trans A 2011;42:239.
[16] Phillion A, Vernède S, Rappaz M, Cockcroft S, Lee PD. Int J Cast Metals Res 2009;22:240.
[17] Vernède S, Jarry P, Rappaz M. Acta Mater 2006;54:4023.
[18] Dijkstra WO, Vuik C, Dammers AJ, Katgerman L. TMS; 2004. p. 151–6.
[19] Sistaninia M, Phillion AB, Drezet JM, Rappaz M. Acta Mater 2012;60:3902.
[20] Sun Z, Log R, Bernacki M. Comput Mater Sci 2010;49:158.
[21] Rappaz M, Jacot A, Boettinger W. Metall Mater Trans A: Phys Metall Mater Sci 2003;34 A:467.
[22] Hasson G, Goux C. Scripta Metall 1971;5:889.
[23] Mathier V, VernFde S, Jarry P, Rappaz M. Metall Mater Trans A 2009;40:943.
[24] Terzi S, Salvo L, SuTry M, Dahle A, Boller E. Trans Nonferr Metals Soc China 2010;20(Suppl. 3):s734.
[25] Vernède S, Rappaz M. Acta Mater 2007;55:1703.

[26] Dongarra J, Lumsdaine R, Pozo R, Remington K. In: Proceedings of the second object oriented numerics conference; 1994. p. 214–8.

[27] Sistaninia M, Phillion A, Drezet JM, Rappaz M. In: 49th Annual conference of metallurgists. Vancouver, BC; 2010.

[28] Phillion A, Thompson S, Cockcroft S, Wells M. Mater Sci Eng : A 2008;497:388.

[29] Meidani H, Desbiolles JL, Jacot A, Rappaz M. Acta Mater 2012;60:2518.

[30] Syvertsen M. Metall Mater Trans B: Process Metall Mater Process Sci 2006;37:495.

[31] Waller I, Ebbsjo I. J Phys C: Solid State Phys 1979;12:705.

[32] Lapshin O, Savitskii A, Ovcharenko V. Sci Sinter 2002;34:203.

[33] Decultieux F. Characterization of the thermomechanical behavior of casting alloys during solidification. PhD thesis, ENS Mines de Paris, Paris; 1996.

[34] Fuloria D, Lee P. Acta Mater 2009;57:5554.

[35] Carman P. Trans Instit Chem Eng 1937;15:150.

[36] Eskin DG, Suyitno, Katgerman L. Prog Mater Sci 2004;49:629.

[37] Magnin B, Maenner L, Katgerman L, Engler S. Mater Sci Forum 1996;217–222:1209.